HHS Public Access

Author manuscript

*Prog Biophys Mol Biol*. Author manuscript; available in PMC 2022 March 01.

Published in final edited form as:

*Prog Biophys Mol Biol*. 2021 March ; 160: 37–42. doi:10.1016/j.pbiomolbio.2020.05.006.

# High Resolution Single Particle Cryo-EM Refinement Using JSPR

**Chen Sun**[1], **Brenda Gonzalez**[1], **Frank S Vago**[1], **Wen Jiang**[1,*]

[1]Department of Biological Sciences, Markey Center for Structural Biology, Purdue University, West Lafayette, IN, 47906, USA

## Abstract

JSPR is a single particle cryo-EM image processing and 3D reconstruction software developed in the Jiang laboratory at Purdue University. It began as a few refinement scripts for symmetric and asymmetric reconstructions of icosahedral viruses, but has grown into a comprehensive suite of tools for building *ab initio* reconstructions, high resolution refinements of viruses, protein complexes of arbitrary symmetries including helical tubes/filaments, and image file handling utilities. In this review, we will present examples achieved using JSPR and demonstrate recently implemented features of JSPR such as multi-aberration “alignments” and automatic optimization of masking for the assessment of map resolution using “true” FSC.

### Keywords

generalized 2D alignments; aberration correction; beam tilt; defocus refinement; phase shift refinement; elliptic distortion

## 1. Introduction

Single particle cryo-EM has revolutionized structural biology in the past few years and become the method of choice for structural biology for a wide range of structures from large (10–100 MDa in mass and ~200 nm in diameter), highly symmetric viruses (Dai and Hong Zhou, 2018; Fang et al., 2019) to small (sub-100 kDa), asymmetric protein or nucleotide structures (Zhang et al., 2019), and helical polymers (Fitzpatrick et al., 2017; Wang et al., 2019). Due to their size, symmetry, and higher signal to noise ratios (SNR) from the stronger electron scattering, icosahedral viruses were among the very few samples that could reach high resolution with cryo-EM (Jiang et al., 2008; Yu et al., 2008; Zhang et al., 2008) before the resolution revolution brought by the development of direct electron detectors. JSPR was initially developed for structure determination of viruses at Purdue University. This includes both symmetric reconstructions of the capsid shell with icosahedral symmetry (Chen et al., 2011; Guo et al., 2014; Jiang et al., 2008) and asymmetric reconstructions of the non-

*Corresponding author (jiang12@purdue.edu).

**Chen Sun:** Writing - Original Draft, Visualization **Brenda Gonzalez:** Writing - Review & Editing **Frank S. Vago:** Writing - Review & Editing **Wen Jiang:** Conceptualization, Methodology, Software, Supervision, Funding acquisition, Writing - Review & Editing

icosahedral structural components of the virus particles such as the phage tail and portal vertex (Guo et al., 2013; Jiang et al., 2006). It began as a few refinement scripts based on EMAN (Ludtke et al., 1999) and EMAN2 (Tang et al., 2007) libraries but has grown into a comprehensive suite of tools for building *ab initio* reconstructions, high resolution refinements of viruses, protein complexes of arbitrary symmetries including helical tubes/filaments, and image file handling utilities. The general workflow from particle picking, CTF fitting, *ab initio* reconstruction using the random model approach, initial orientation determination using a consensus voting criterion, 3D reconstruction, and iterative refinements was previously detailed (Guo and Jiang, 2014). In this review, we will focus on high resolution refinement functions in JSPR, and useful image handling and parameter manipulation tools used to help translate data among various software packages, such as RELION (Scheres, 2012), and cryoSPARC (Punjani et al., 2017).

## 2. Generalized multi-aberration 2D alignment in addition to Euler angles and center positions

In single particle cryo-EM image processing, the 2D alignment step of the iterative refinement loop typically included only either a global search, or local refinement of particle Euler angles and center positions. The contrast transfer function (CTF) parameters of the particles, including defocus, astigmatism magnitude and angles, and phase shifts (if a phase plate was used), are pre-determined using the whole micrograph power spectra or smaller patches around the particles. This workflow is based on an implicit assumption that CTF fitting results were infinitely accurate. This assumption is obviously invalid or at least suboptimal as the power spectra-based CTF fitting methods have discarded a majority of the image information, such as phase. To more accurately determine CTF parameters and other aberration parameters, we generalized the Euler/center-only 2D alignment to also “align” these parameters as part of the iterative refinement process (Fig. 1A) (Guo and Jiang, 2014), which can take advantage of all the information of the particle images and the iteratively improved reference map quality.

We previously implemented different “aligners”, where each aligner is refining one (for example, defocus or phase shift), or a few closely related parameters (such as astigmatism amplitude/angle or elliptic distortion amplitude/angle) (Guo and Jiang, 2014). The different aligners can be combined in user defined order during 2D alignment. More recently, a new aligner, *refineAll*, was developed to allow simultaneous refinement of all or a subset of the parameters, which improved alignment quality and also eliminated the need for the user to find the best order of sequential alignments. The parameters that *refineAll* supports include Euler angle, center, defocus, astigmatism, phase shift, beam tilt, spherical aberration, pixel size, and elliptic distortion. Users can easily turn on/off the refinement of any parameters and choose the refinement at the per particle or per micrograph level.

The refinement of aberration parameters has been shown not only to noticeably improve the reconstruction resolution, but sometimes essential to reach near-atomic resolution (4 Å and better) when aberrations are large. For example, the porcine circovirus 2 (PCV2) structure (Liu et al., 2016) was limited to 3.3 Å with only Euler/center refinement, but improved to

2.9 Å with aberration refinement/correction (Fig. 1B). While individual aberration correction could slightly improve the resolution, the holistic effect of multi-aberration corrections led to improvements in resolution (Fig. 1B) and side-chain densities (Fig. 2G).

A perfect imaging system would be free of aberrations, but in practice, all TEMs have residual aberrations either due to the fundamental limit of the magnetic lens optics, or misalignment of the lens and lens correctors (Hawkes, 2015). Elliptical distortion is a lens distortion caused by differing magnetic field strengths in the projection lenses in various directions. While TEM vendors generally correct the distortions for high magnifications (>40k) traditionally used for high resolution imaging, lower magnifications (<30k), often used with a K2 direct electron detector due to its small pixel size (5 μm), were found to have ~2–3% elliptic distortion (Yu et al., 2016b). While low amounts of elliptical distortion are ignorable for studies of smaller protein targets, elliptical distortion correction for larger targets, such as viruses (Fig. 1C), is essential (Yu et al., 2016b). For example, the T4 head structure was limited to ~7 Å resolution, but was improved to 3.3 Å resolution after elliptical distortion correction (Chen et al., 2017). The distortion parameters were determined as part of the 2D alignment, eliminating the need for pre-calibration which might not be feasible after data collection.

Beam tilt induced coma aberrations were first found to be significant in processing 2D crystal images (Henderson et al., 1986), but has now also been recognized as an important parameter in refinement for high resolution single particle cryo-EM (Glaeser et al., 2011). In our recent study on Volta phase plate imaging, we have collected a dataset with severe beam tilt that was accidentally introduced during data collection, likely because of an unknown software glitch (Li et al., 2019). Without beam tilt correction, the reconstruction was limited to ~6 Å resolution and the Fourier shell correlation (FSC) curve had multiple large oscillations (Fig. 1D). We quickly identified the large beam tilt issue with the *refineAll* aligner in JSPR after we observed the reduction of oscillations in the FSC curve post beam tilt refinement/correction (Fig. 1D). The final resolution of 2.5 Å was achieved after additional multi-aberration refinement/correction (Li et al., 2019).

## 3. High resolution structures determined using JSPR

Most of the initial work with JSPR was done with virus reconstruction. As the scope of the projects began to expand beyond viruses, JSPR has been used to solve the structures of protein complexes and helical polymers. A few structures determined using JSPR will be briefly described here.

### Viruses.

Figure 2 shows a gallery of virus structures solved with JSPR in recent years. The 2.9 Å PCV2 structure (Fig. 2A) (Liu et al., 2016) has demonstrated the possibility of high resolution reconstruction with close-packed particles. It is also the first and only sub-3 Å structure (Fig. 1B) using photographic film. The 3.8 Å Zika virus structure (Fig. 2B) (Sirohi et al., 2016) provides a foundation for analysis of the antigenicity and pathogenesis of Zika virus. The 2.6 Å Tulane virus structure (Fig. 2C) (Yu et al., 2016a) demonstrated the feasibility of achieving high resolution reconstructions using antibody-based affinity grids to

enrich low concentration particles on the EM grid. The 2.3 Å structure of human rhinovirus B14 with C5 antibody Fab (Fig. 2D) (Dong et al., 2017) depicts the highest resolution of a virus-antibody complex. The 3.3 Å T4 phage head structure (Chen et al., 2017) (Fig. 2E) highlighted the severe negative impact of elliptic distortion on large structures and the dramatic improvement of the resolution from ~7 Å to 3.3 Å by elliptic distortion correction using JSPR. The 2.9 Å bacteriophage Sf6 structure (Fig. 2F) (Zhao et al., 2017) was the first tailed phage structure determined to sub-3 Å resolution.

### Protein complexes.

It is sometimes misunderstood that JSPR only supports icosahedral viruses, probably due to our previous work mainly featuring viruses. However, JSPR supports all point-group symmetries including all platonic solids (I, O, and T symmetries), dihedral symmetries (D), cyclic symmetries (C), and no symmetry. Figure 3A shows the 2.7 Å structure of the T20S proteasome submitted to the 2016 map challenge (emcd108). The two JSPR maps submitted to the map challenge (this T20S structure and emcd132 for GroEL) were assessed among the best density maps (Heymann et al., 2018; Marabini et al., 2018; Pintilie and Chiu, 2018) and the assessors included comments such as, “JSPR is always among the best” (Marabini et al., 2018). In a recent study using the Volta phase plate, a 2.5 Å apoferritin structure (Li et al., 2019) (Fig. 3B) was obtained with JSPR after refining and correcting large beam tilts accidentally introduced during data collection (Fig. 1D). We have also refined the asymmetric ribosome structure, EMPIAR-10107 (Desai et al., 2017), to ~3 Å with JSPR (Fig. 3C). These examples demonstrated the capability of JSPR for reconstructing non-virus structures.

### Helical polymers.

Support for helical structures using the Iterative Helical Real Space Reconstruction (IHRSR) strategy (Egelman, 2007) was recently added to JSPR. The “gold standard” split of a dataset is done at the micrograph or filament/tube level instead of the particle (i.e. helical segment) level to avoid inflated FSCs due to the same region of pixels in neighboring but overlapping segments being separated into different subsets. Figure 3D shows a ~3 Å structure of the VipA/VipB protomer Type VI secretion system contractile sheath (EMPIAR-10019) (Kudryashev et al., 2015) with both *de novo* indexing and refinement by JSPR. The new helical indexing and classification method will be published separately.

## 4. Utilities in JSPR

JSPR is currently a CPU-based image processing software that runs on Linux-based computing environments, an ad hoc collection of workstations, CPU cycle-scavenging HTCondor (Jiang et al., 2008), and dedicated Linux clusters managed by a job queue system, such as PBS or Slurm. It has been programmed in a way that whenever an unexpected stop occurs, it is able to automatically resume at the last stopping point. This is realized by dividing large tasks, for example, the 2D alignment, into batches and tracking the completion state of each batch.

In addition to the iterative refinement function, JSPR also includes a rich set of utilities that facilitate analysis of the refinement results and interchanges of results with other image processing software. Here we only briefly describe three such utilities while a more comprehensive list of utilities is available in the software that is freely downloadable from the corresponding author's website (https://jiang.bio.purdue.edu/jspr).

### images2lst.py and images2star.py.

Both programs were initially designed to convert files from different software packages, for example, cisTEM's database (**.db*) file or cryoSPARC's (**.cs*) file, into *lst* file used by JSPR or *star* file used by RELION, and to allow interchanging between JSPR and RELION. Later, they were enhanced with many additional functions. For example, it allows users to easily check/remove duplicate particles, add parameters to a *lst/star* file, copy parameters from another *lst/star* file, perform subset selection based on the desired range of any parameters, perform symmetry expansion or the reverse, remove excessive number of particles in the dominant views, subtract projections with real space linear scaling of pixel levels or Fourier space per resolution shell amplitude scaling, or virtually shift reconstruction center position for localized reconstruction of arbitrary sizes without the need to re-extract/clip the particles into another dataset, *etc*.

### plotDist.py.

This script allows the user to plot the histogram of arbitrary parameters or the correlation of any pair of parameters in a *lst* or *star* file and the plot can be interactively examined or saved into a PDF file. These plots are useful in evaluating data (e.g., distribution of defocus values) or the refinement behavior (e.g., distribution of Euler angle changes or how Euler angle changes are correlated to defocus value changes, *etc*.).

### trueFSC.py.

Although FSC has been widely used for the estimation of the cryo-EM map resolution after its first introduction (Harauz and van Heel, 1986), how to properly mask out the background (i.e. solvent flattening) is often a dilemma as the FSC tends to report different resolution values with different levels of masking. If the mask is too tight, the resolution will be overestimated because of the mask correlation at high resolution. If the mask is too loose, the resolution will be underestimated, which means the map quality is better than the reported resolution. An optimal mask should contain all protein pixels, exclude background/noise pixels as much as possible, and use a soft transition layer (i.e. tapering) of appropriate slope between the protein and background regions. The masking is typically based on a thresholding method for which the quality of masking is critically dependent on the threshold value. Current software still requires the user to manually input the threshold for mask generation, which can be tedious and often leads to suboptimal masking. To address this problem, we developed a python script, *trueFSC.py*, which can automatically find the best threshold and mask slope for reliable resolution estimation. The user only needs to specify the two half maps. A plot of the FSC curves in PDF format and two masks for the half maps will be generated. There are two different methods for automatic threshold determination that have been implemented. The preferred approach is to specify the mass of the protein complex, which is used to calculate a threshold to make the total volume of all

pixels with larger values equal to the expected volume assuming an average protein density (1.35 g/cm$^3$) (Fischer et al., 2004). The second automatic threshold determination method is based on Otsu's thresholding method that automatically finds a cutoff value so that the variances within the two groups are minimum (Otsu, 1979). Starting from a sharp mask based on the threshold, *trueFSC.py* will then extend it with a soft slope (raised cosine, $\frac{1+cos(r)}{2}$ in which $r$ is the total width of the slope) at an optimal slope width that maximizes the resolution without inflating the FSC of phase randomized maps (Chen et al., 2013). Figure 4A shows an example of a *trueFSC.py* generated FSC and the corresponding soft mask. As a comparison, a large spherical mask will underestimate the resolution (Fig. 4B) while an overly-tight mask will inflate the resolution, as indicated by the inflated FSC of phase randomized maps using the same tight mask (Fig. 4C). We expect this feature will provide a more convenient and accurate FSC calculation, plotting, and resolution reporting tool that can benefit the cryo-EM community.

## 5. Conclusion

The highlight of JSPR is the refinement and correction of multiple aberrations, including CTF parameters and geometric scaling/distortions, which have slowly been recognized in the field. We are happy to see other software packages, for example, cryoSPARC 2.12 and RELION 3.1 (Zivanov et al., 2019), now also include similar functions in their recent updates. Currently, high resolution refinement in JSPR is limited by the homogeneity of the sample. Future developments will need to address the heterogenous states, especially the continuously varying conformations due to the intrinsic dynamics of the structure. While a definite solution is still to be found, an attractive concept is to picture the distribution of particles as a lower-dimension manifold embedded in the hyperspace with dimensions equal to the number of pixels in a particle image (Frank and Ourmazd, 2016). While the manifold for a homogenous set of particles will have only three dimensions for the particles views, the manifold for heterogeneous particles will have additional dimensions to represent the conformations with the number of extra-dimensions ranging from small for simple one or few hinge motions to large for continuously varying conformations throughout the structure. Algorithms based on either classic machine learning methods (Frank and Ourmazd, 2016) or the more recent deep neural networks approach (Zhong et al., 2019) can be explored to learn the manifold.

## Acknowledgement

This work was supported in part by grants from NIGMS U24 GM116789, NIAID R01 AI111095, NINDS 1U01NS110437 to W.J. We thank the Rosen Center for Advanced Computing (RCAC) (https://www.rcac.purdue.edu) here at Purdue University for providing the computing resources for the development and application of JSPR.

## References

Chen S, McMullan G, Faruqi AR, Murshudov GN, Short JM, Scheres SHW, Henderson R, 2013. High-resolution noise substitution to measure overfitting and validate resolution in 3D structure determination by single particle electron cryomicroscopy. Ultramicroscopy 135, 24–35. [PubMed: 23872039]

Chen Z, Sun L, Zhang Z, Fokine A, Padilla-Sanchez V, Hanein D, Jiang W, Rossmann MG, Rao VB, 2017. Cryo-EM structure of the bacteriophage T4 isometric head at 3.3-Å resolution and its relevance to the assembly of icosahedral viruses. Proc. Natl. Acad. Sci. U. S. A 114, E8184–E8193. [PubMed: 28893988]

Dai X, Hong Zhou Z, 2018. Structure of the herpes simplex virus 1 capsid with associated tegument protein complexes. Science 360, eaao7298. [PubMed: 29622628]

Desai N, Brown A, Amunts A, Ramakrishnan V, 2017. The structure of the yeast mitochondrial ribosome. Science 355, 528–531. [PubMed: 28154081]

Dong Y, Liu Y, Jiang W, Smith TJ, Xu Z, Rossmann MG, 2017. Antibody-induced uncoating of human rhinovirus B14. Proc. Natl. Acad. Sci. U. S. A 114, 8017–8022. [PubMed: 28696310]

Egelman EH, 2007. The iterative helical real space reconstruction method: surmounting the problems posed by real polymers. J. Struct. Biol 157, 83–94. [PubMed: 16919474]

Fang Q, Zhu D, Agarkova I, Adhikari J, Klose T, Liu Y, Chen Z, Sun Y, Gross ML, Van Etten JL, Zhang X, Rossmann MG, 2019. Near-atomic structure of a giant virus. Nat. Commun 10, 388. [PubMed: 30674888]

Fischer H, Polikarpov I, Craievich AF, 2004. Average protein density is a molecular-weight-dependent function. Protein Sci. 13, 2825–2828. [PubMed: 15388866]

Fitzpatrick AWP, Falcon B, He S, Murzin AG, Murshudov G, Garringer HJ, Crowther RA, Ghetti B, Goedert M, Scheres SHW, 2017. Cryo-EM structures of tau filaments from Alzheimer's disease. Nature 547, 185. [PubMed: 28678775]

Frank J, Ourmazd A, 2016. Continuous changes in structure mapped by manifold embedding of single-particle data in cryo-EM. Methods 100, 61–67. [PubMed: 26884261]

Glaeser RM, Typke D, Tiemeijer PC, Pulokas J, Cheng A, 2011. Precise beam-tilt alignment and collimation are required to minimize the phase error associated with coma in high-resolution cryo-EM. J. Struct. Biol 174, 1–10. [PubMed: 21182964]

Goddard TD, Huang CC, Meng EC, Pettersen EF, Couch GS, Morris JH, Ferrin TE, 2018. UCSF ChimeraX: Meeting modern challenges in visualization and analysis. Protein Sci. 27, 14–25. [PubMed: 28710774]

Guo F, Jiang W, 2014. Single Particle Cryo-electron Microscopy and 3-D Reconstruction of Viruses, in: Kuo J (Ed.), Electron Microscopy, Methods in Molecular Biology. Humana Press, Totowa, NJ, Totowa, NJ, pp. 401–443.

Harauz G, van Heel M, 1986. Exact filters for general geometry three dimensional reconstruction. sbio.uct.ac.za 73, 146–156.

Hawkes PW, 2015. The correction of electron lens aberrations. Ultramicroscopy 156, A1–64. [PubMed: 26025209]

Henderson R, Baldwin JM, Downing KH, Lepault J, Zemlin F, 1986. Structure of purple membrane from halobacterium halobium: recording, measurement and evaluation of electron micrographs at 3.5 Å resolution. Ultramicroscopy 19, 147–178.

Heymann JB, Marabini R, Kazemi M, Sorzano COS, Holmdahl M, Mendez JH, Stagg SM, Jonic S, Palovcak E, Armache J-P, Zhao J, Cheng Y, Pintilie G, Chiu W, Patwardhan A, Carazo J-M, 2018. The First Single Particle Analysis Map Challenge: A Summary of the Assessments. J. Struct. Biol 10.1016/j.jsb.2018.08.010

Jiang W, Baker ML, Jakana J, Weigele PR, King J, Chiu W, 2008. Backbone structure of the infectious epsilon15 virus capsid revealed by electron cryomicroscopy. Nature 451, 1130–1134. [PubMed: 18305544]

Kudryashev M, Wang RY-R, Brackmann M, Scherer S, Maier T, Baker D, DiMaio F, Stahlberg H, Egelman EH, Basler M, 2015. Structure of the type VI secretion system contractile sheath. Cell 160, 952–962. [PubMed: 25723169]

Li K, Sun C, Klose T, Irimia-Dominguez J, Vago FS, Vidal R, Jiang W, 2019. Sub-3 Å apoferritin structure determined with full range of phase shifts using a single position of volta phase plate. J. Struct. Biol 206, 225–232. [PubMed: 30928614]

Liu Z, Guo F, Wang F, Li T-C, Jiang W, 2016. 2.9 Å Resolution Cryo-EM 3D Reconstruction of Close-Packed Virus Particles. Structure 24, 319–328. [PubMed: 26777413]

Ludtke SJ, Baldwin PR, Chiu W, 1999. EMAN: semiautomated software for high-resolution single-particle reconstructions. J. Struct. Biol 128, 82–97. [PubMed: 10600563]

Marabini R, Kazemi M, Sorzano COS, Carazo JM, 2018. Map Challenge: Analysis using a Pair Comparison Method based on Fourier Shell Correlation. J. Struct. Biol 10.1016/j.jsb.2018.09.009

Otsu N, 1979. A threshold selection method from gray-level histograms. IEEE Trans. Syst. Man Cybern 9, 62–66.

Pintilie G, Chiu W, 2018. Assessment of Structural Features in Cryo-EM Density Maps using SSE and Side Chain Z-Scores. J. Struct. Biol 10.1016/j.jsb.2018.08.015

Sirohi D, Chen Z, Sun L, Klose T, Pierson TC, Rossmann MG, Kuhn RJ, 2016. The 3.8 Å resolution cryo-EM structure of Zika virus. Science 352, 467–470. [PubMed: 27033547]

Tang G, Peng L, Baldwin PR, Mann DS, Jiang W, Rees I, Ludtke SJ, 2007. EMAN2: an extensible image processing suite for electron microscopy. J. Struct. Biol 157, 38–46. [PubMed: 16859925]

Wang F, Gu Y, O'Brien JP, Yi SM, Yalcin SE, Srikanth V, Shen C, Vu D, Ing NL, Hochbaum AI, Egelman EH, Malvankar NS, 2019. Structure of Microbial Nanowires Reveals Stacked Hemes that Transport Electrons over Micrometers. Cell 177, 361–369.e10. [PubMed: 30951668]

Yu G, Li K, Huang P, Jiang X, Jiang W, 2016a. Antibody-Based Affinity Cryoelectron Microscopy at 2.6-Å Resolution. Structure 24, 1984–1990. [PubMed: 27806259]

Yu G, Li K, Liu Y, Chen Z, Wang Z, Yan R, Klose T, Tang L, Jiang W, 2016b. An algorithm for estimation and correction of anisotropic magnification distortion of cryo-EM images without need of pre-calibration. J. Struct. Biol 195, 207–215. [PubMed: 27270241]

Zhang K, Li S, Kappel K, Pintilie G, Su Z, Mou T-C, Schmid MF, Das R, Chiu W, 2019. Cryo-EM structure of a 40 kDa SAM-IV riboswitch RNA at 3.7 Å resolution. Nat. Commun 10, 5511. [PubMed: 31796736]

Zhao H, Li K, Lynn AY, Aron KE, Yu G, Jiang W, Tang L, 2017. Structure of a headful DNA-packaging bacterial virus at 2.9 Å resolution by electron cryo-microscopy. Proc. Natl. Acad. Sci. U. S. A 114, 3601–3606. [PubMed: 28320961]

Zhong ED, Bepler T, Davis JH, Berger B, 2019. Reconstructing continuous distributions of 3D protein structure from cryo-EM images. arXiv [q-bio.QM]

Zivanov J, Nakane T, Scheres SHW, 2019. Estimation of High-Order Aberrations and Anisotropic Magnification from Cryo-EM Datasets in RELION-3.1. bioRxiv. 10.1101/798066

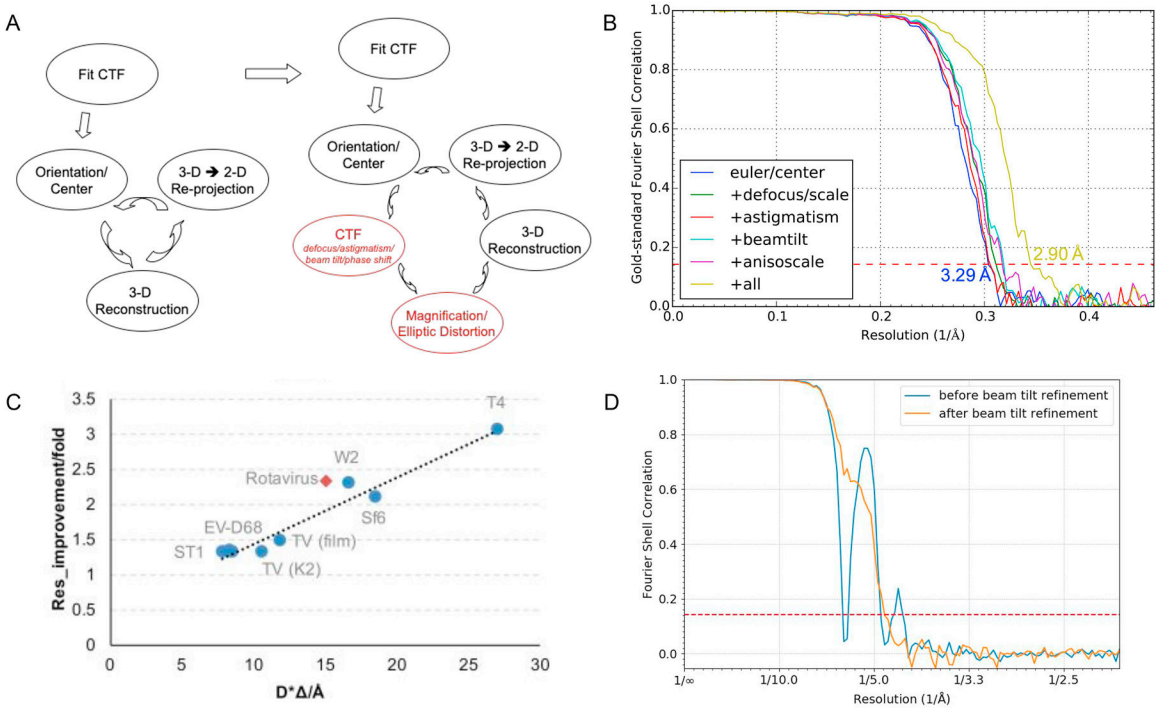


**Figure 1. Generalized multi-aberration 2D alignment in JSPR.**

(A) The iterative refinement loop “aligns” multiple CTF parameters and geometric parameters in addition to the particle Euler angles and center positions. (B) Multi-aberration refinements improved the PCV2 structure from 3.3 Å to 2.9 Å resolution (Liu et al., 2016). The “anisoscale” parameter in the legend means elliptic distortion correction. (C) Correction of elliptic distortion could significantly improve the resolution of large viruses (Yu et al., 2016b). (D) The beam tilt induced coma aberrations can be corrected as indicated by the reduction of the large oscillations in the FSC curve (Li et al., 2019). (B, C, D) have been reproduced with the permission of the corresponding publishers.

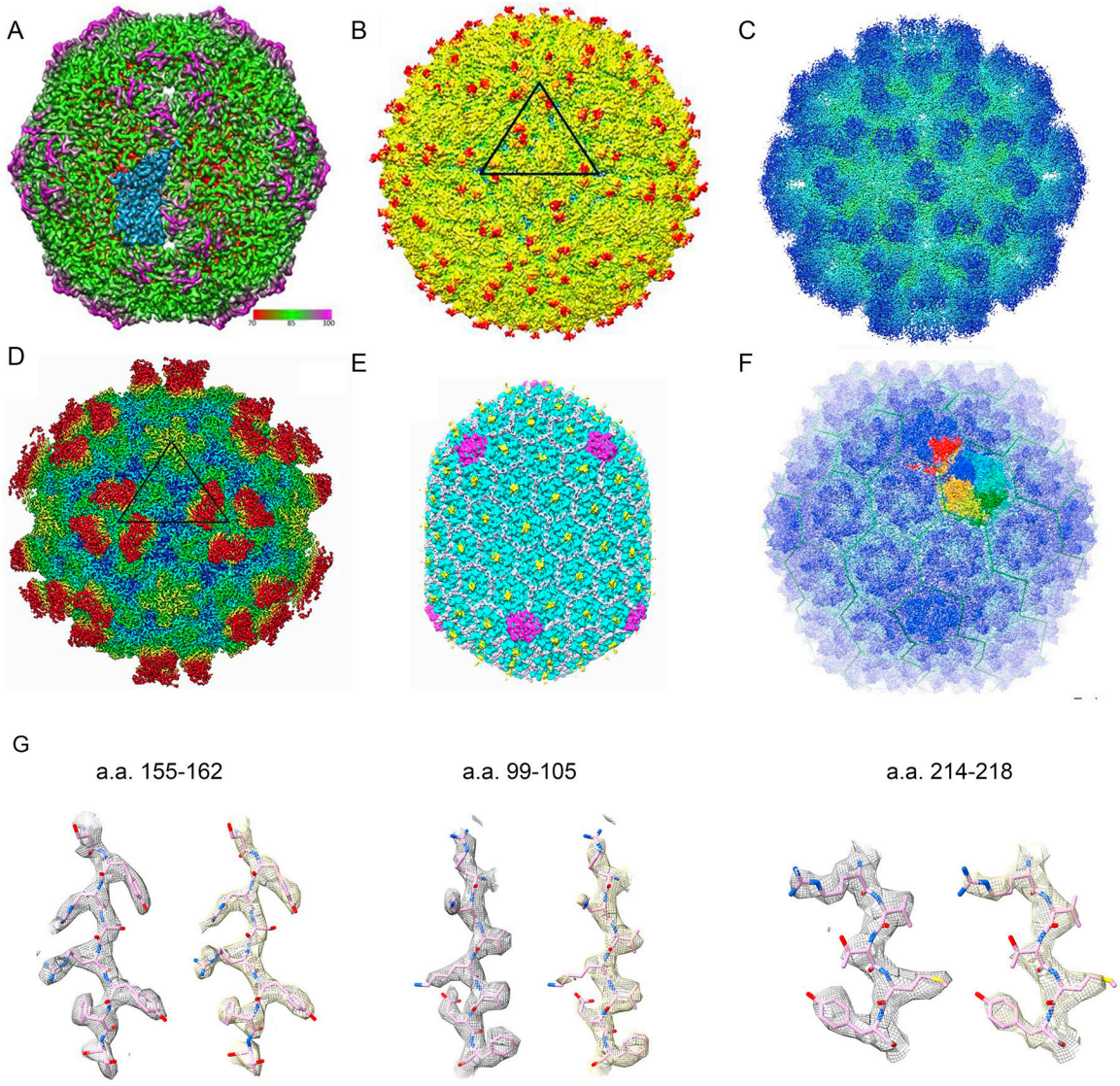


**Figure 2. Gallery of high resolution virus structures reconstructed with JSPR.**

(A) 2.9 Å PCV2 structure (EMD-6555) using images recorded on photographic film (Liu et al., 2016). (B) 3.8 Å Zika virus structure (EMD-8116) (Sirohi et al., 2016). (C) 2.6 Å Tulane virus (EMD-8252) (Yu et al., 2016a). (D) 2.3 Å human rhinovirus B14 and antibody complex (EMD-8762) (Dong et al., 2017). (E) 3.3 Å bacteriophage T4 isometric head (EMD-8661) (Chen et al., 2017). (F) 2.9 Å bacteriophage Sf6 (EMD-8314) (Zhao et al., 2017). (G) The comparison of the side chain densities of PCV2 in maps with all the refinement parameters (left, grey mesh) and only the Euler/center parameters (right, yellow mesh) in three regions, a.a. 155–162, a.a. 99–105, and a.a. 214–218, superimposed with the PCV2 model (PDB:3JCI). The two density maps have been sharpened to the same level and displayed at the same contour level using ChimeraX (Goddard et al., 2018). (A-F) have been reproduced with the permission of the corresponding publishers.

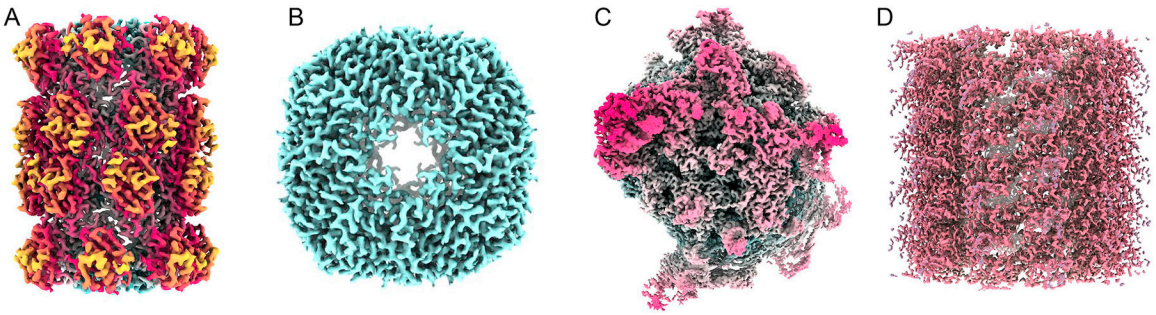


**Figure 3. Gallery of high resolution non-virus structures reconstructed with JSPR.**

(A) 2.7 Å T20S proteasome structure submitted to the 2016 Cryo-EM Map Challenge (emcd108). (B) 2.5 Å apoferritin structure from Volta phase plate data (Li et al., 2019). (C) 3 Å ribosome structure solved using the EMPIAR-10107 dataset (Desai et al., 2017). (D) 3 Å VipA/VipB helical structure reconstructed from the EMPIAR-10019 dataset (Kudryashev et al., 2015).

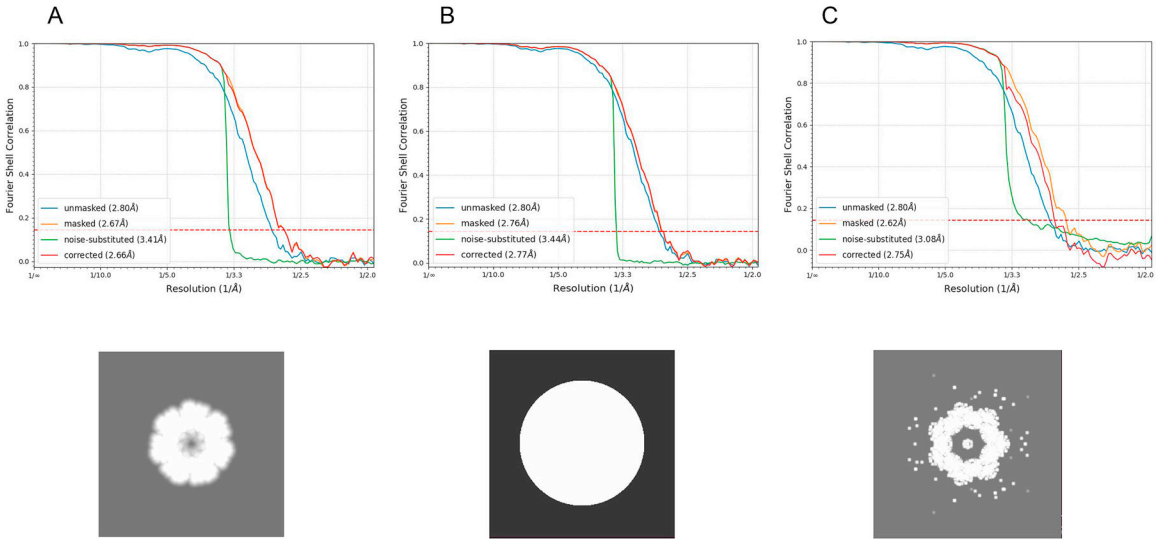


**Figure 4. Examples of different levels of masking and their effect on FSC curves.**

(A) Reliable resolution estimate using the optimal mask automatically determined by *trueFSC.py*. (B) Large spherical mask underestimates the resolution. (C) Overly tight mask inflates the resolution if the FSC=0.143 criterion is applied directly to the FSC of masked maps (2.62 Å). The large FSC values beyond the phase randomization cutoff resolution (~3.4 Å) in the noise-substituted map FSC curve (green) provide clear signs that the mask is too tight.